ARTICLE

Check for updates

Local resonance bandgap control in a particle-aligned magnetorheological metamaterial

Mohammadreza Moghaddaszadeh [1,2,8], Andrew Ragonese[1,8], Yong Hu [1,8], Zipeng Guo [3,4,5,8], Amjad Aref[2], Chi Zhou [3], Shenqiang Ren[1,6,7] & Mostafa Nouh [1,2 ✉]

Stimuli-responsive elastic metamaterials augment unique subwavelength features and wave manipulation capabilities with a degree of tunability, which enables them to cut across different time scales and frequency regimes. Here, we present an experimental framework for robust local resonance bandgap control enabled by enhanced magneto-mechanical coupling properties of a magnetorheological elastomer, serving as the resonating stiffness of a metamaterial cell. During the curing process, ferromagnetic particles in the elastomeric matrix are aligned under the effect of an external magnetic field. As a result, particle chains with preferred orientation form along the field direction. The resulting anisotropic behavior significantly boosts the sensitivity of the metamaterial's elastic modulus to the imposed field during operation, which is then exploited to control the dispersive dynamics and experimentally shift the location and width of the resonance-based bandgap along the frequency axis. Finally, numerical simulations are used to project the performance of the magnetically-tunable metamaterial at stronger magnetic fields and increased levels of material anisotropy, as a blueprint for broader implementations of in situ tunable active metamaterials.

[1] Department of Mechanical and Aerospace Engineering, University at Buffalo (SUNY), Buffalo, NY 14260, USA. [2] Department of Civil, Structural and Environmental Engineering, University at Buffalo (SUNY), Buffalo, NY 14260, USA. [3] Department of Industrial and Systems Engineering, University at Buffalo (SUNY), Buffalo, NY 14260, USA. [4] Department of Industrial and Systems Engineering, Rochester Institute of Technology, Rochester, NY 14623, USA. [5] AMPrint Center, Rochester Institute of Technology, Rochester, NY 14623, USA. [6] Department of Chemistry, University at Buffalo (SUNY), Buffalo, NY 14260, USA. [7] Department of Materials Science and Engineering, University of Maryland, College Park, MD 20742, USA. [8] These authors contributed equally: Mohammadreza Moghaddaszadeh, Andrew Ragonese, Yong Hu, Zipeng Guo. ✉email: mnouh@buffalo.edu

Elastic metamaterials and metasurfaces are artificially engineered materials with resonance-based features that enable wave control and manipulation at a subwavelength scale[1,2]. Over the past two decades, they have demonstrated extraordinary capabilities in wave guidance[3], steering[4–6], energy harvesting[7], analog computing[8], and nonreciprocal wave propagation[9], to name a few. At the heart of the vast majority of metamaterial applications is the ability to absorb wave propagation within bounded frequency windows, commonly known as bandgaps (BGs). These BGs typically emerge as a result of destructive interferences at the interface of impedance-mismatched materials in periodic crystals[10], typically referred to as Bragg bandgaps, or as a result of resonance scattering and hybridization in structures hosting internal resonators[11]; the latter being the focus of this work.

Unlike Bragg effects, mechanical resonances rely solely on mass and stiffness features rendering them unit-cell-size-independent, which enable local resonance BGs to extend to low frequency regimes (as low as 0.25 kHz as will be shown here) which are of critical importance to a wide range of vibroacoustic applications, without resorting to unrealistically large geometries. Despite the promise of a strong low-frequency attenuation, the potential of local resonance BGs remains largely untapped due to their narrow frequency range. As a result, a spurt of efforts have shared a common theme of exploring novel (passive) configurations of elastic metamaterials which exhibit wider gaps and broader dispersive characteristics. Notable among these are designs which involve interactions of neighboring[12], non-local resonators[13], and dual-periodic resonators[14], origami designs[15], as well as inertant metamaterials[16]. In tandem, the notion of BG control has surfaced as a means to tune the location (i.e., starting frequency) and width (i.e., spanned frequency range) of such local resonance bandgaps. In structural form, locally resonant unit cells are typically comprised of three components: a host matrix, a filler material, and a near-rigid core[17,18]. As such, BG tunability can be potentially addressed via two distinct approaches: (1) Reconfigurable geometries[19–21] and (2) Response to external stimulus[22–24]. The latter uniquely positions metamaterials in rapidly changing environments given the ability of stimuli-responsive materials to be effectively tuned in real time. With recent advances in additive manufacturing, BG control has been exhibited in molecular ferroelectric metamaterials[25]. This work experimentally demonstrates robust local resonance bandgap control in a 3D-printed magnetorheological metamaterial through rigorous tuning of its anisotropic elastic profile.

Owing to their rapid, reversible tunability and long lifetimes, magnetorheological elastomers (MREs) are good candidates for active structural design. MRE composites are formed by homogeneously mixing and curing ferromagnetic particles, additives, and elastomer matrices[26]. Their mechanical properties, including the elastic (Young's) modulus, can be tuned on the order of milliseconds by applying an external magnetic field due to magneto-mechanical coupling[27–29]. Aside from lattice buckling[30] and reconfiguration of internal architectures[31], MRE-based metamaterials exploit stiffness variations as a function of external magnetic stimulation to achieve BG control. This was successfully implemented in phononic crystals, both theoretically[32–34] and experimentally[35]. In resonant metamaterials, MREs have been theoretically used as a cladding layer (filler) in unit cells, adding a degree of tunability to the central position and width of the formed BGs[36], an idea which was further expanded by adding a micro-electromagnetic coil as a core element and tuning the resonant frequency by adjusting the coil-induced magnetic field[37]. These theoretical concepts were first translated to a physically printed magneto-active system using direct-ink writing[38], and later used to break space inversion symmetry in lattice designs inspired by the morphology of graphene bilayers[39].

In this work, we demonstrate the significance of magnetic particle alignment in the elastomeric MRE matrix and its profound effect on the magneto-mechanical coupling and ensuing BG tunability of the stimulus–responsive metamaterial. Isotropic MREs, henceforth referred to as "non-aligned" MREs, are fabricated in the absence of magnetic field alignment. In the resultant configuration, magnetic particles are uniformly distributed. When particles are aligned under a magnetic field during the curing process, particle chains with preferred orientation form along the magnetic field direction, resulting in a class of anisotropic MREs[40], henceforth termed as "aligned" MREs. The emergent anisotropy notably enhances the coupling process. Here, we synthesize and exploit the strong magneto-mechanical coupling of aligned MREs to achieve strong local resonance bandgap control in a magnetically activated metamaterial with a 3D-printed mold and a magnetorheological filler, as depicted and summarized in Fig. 1.

Results

Magneto-mechanical coupling. To evaluate the effect of magnetic anisotropy (the directional dependence of the material's magnetic properties) on the magneto-mechanical coupling of the MRE, non-aligned and aligned MRE samples were fabricated. All properties are summarized in the Materials section. Scanning electron microscopy (SEM) and energy dispersive X-ray spectroscopy (EDS) mapping measurements were conducted to understand the anisotropic magnetic behavior (refer to the Measurements section for details). As shown in Fig. 2d, the carbonyl iron particles are aligned in the elastomeric medium for the aligned MRE as a result of the magnetic field imposed during the curing process. In contrast, the non-aligned MRE does not report a noticeable anisotropic magnetic behavior as carbonyl iron particles are uniformly distributed in the elastomeric medium (Fig. 2a). The magnetization–hysteresis (M–H) loops for non-aligned and aligned MREs are measured as shown in Fig. 2b, e, respectively. Contrary to the non-aligned MRE, the aligned sample demonstrates an obvious anisotropic behavior with a large saturation magnetization of 133 emu g^{-1} (Fig. 2e). To evaluate the role of the aforementioned anisotropy in the stiffness tunability of an elastic medium, local resonance BG shift in a locally resonant metamaterial with a tunable MRE filler (Fig. 1c) in the absence and presence of a magnetic field is shown in Fig. 2c, f corresponding to non-aligned and aligned resonant fillers, respectively. The metamaterial houses a total of 16 unit cells lined up over 2 rows. Owing to weak magneto-mechanical coupling in the non-aligned case, the observable BG shift depicted in Fig. 2f is lacking in Fig. 2c. The saturation magnetic field (i.e., minimum field to saturate the magnetization) increases continuously as a result of changing the magnetic field angle from 0° to 90° (i.e., from a position parallel to one perpendicular to the aligned magnetic field), and decreases thereafter, as shown in Fig. 3a. Specifically, the change in saturation magnetic field is 0%, 53%, and 3% for 0°, 90°, and 180°, respectively. The coercivity also shows continuous change as the measuring magnetic field direction is rotated. As shown in Supplementary Fig. S1, the coercivity change is 0%, 11.2%, and −0.3% for 0°, 90°, and 180°, respectively. Control experiments for the non-aligned MRE show a lack of change in both the saturation magnetic field and coercivity as can be seen in Fig. 3a and Supplementary Fig. S1, respectively. The magneto-mechanical coupling is further studied via in situ compression tests (see the Measurements section for details). Stress-strain curves for the aligned MRE under different magnetic fields confirm an increase in Young's modulus with an
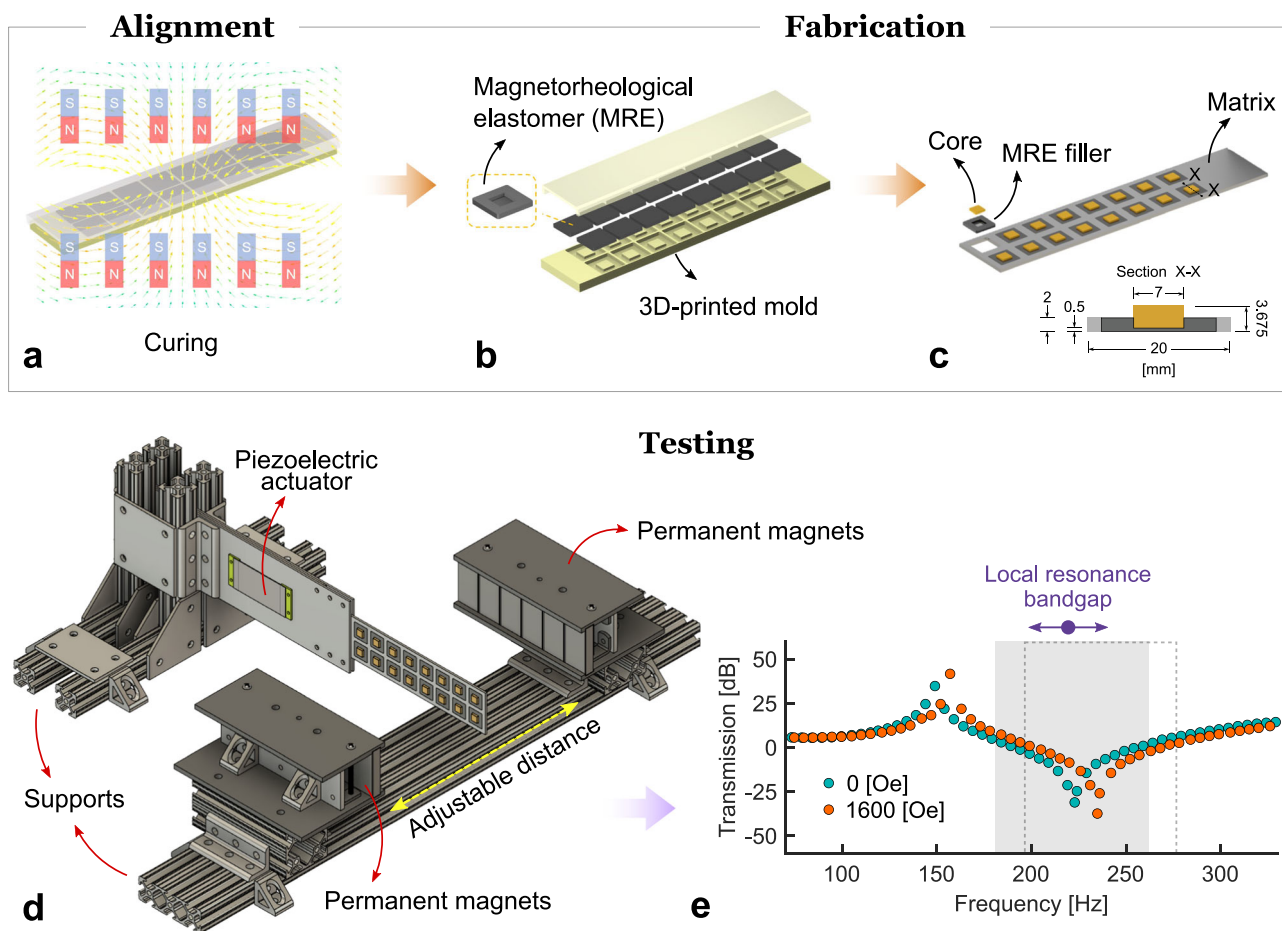
Fig. 1 An anisotropic MRE-based locally resonant metamaterial. a Ferromagnetic particle alignment during the curing process to induce magnetic anisotropy. **b** Metamaterial fabrication via a 3D-printed mold. **c** Integration of outer matrix, resonating core, and tunable magnetorheological filler. **d** Experimental apparatus and magnetic field strength variation via adjustable distance between facing magnets. **e** Transmission spectrum and local resonance bandgap control in the absence and presence of magnetic field.

increase in the applied magnetic field (Supplementary Fig. S2). Figure 3b summarizes the measured moduli for the aligned MREs at 0, 850, 1300, and 1600 Oe to be 1.08, 1.11, 1.21, and 1.27 MPa, respectively. As expected, the non-aligned samples show smaller changes in Young's modulus due to the isotropic magnetic behavior (Supplementary Fig. S2). The obtained moduli for the non-aligned MRE are 0.43 and 0.41 MPa for 0 and 1600 Oe, respectively. In addition to the reported changes in the modulus value, it is noted here that the alignment process also significantly enhances Young's modulus.

MRE-based anisotropic metamaterial. An elastic metamaterial is fabricated using a locally resonant unit cell consisting of an aligned MRE membrane (resonator spring) which fills an outer aluminum matrix and houses a brass core (resonator mass), as shown in Fig. 4a. The resonator sits on a very thin layer of the MRE material which provides additional adhesion needed to secure the resonator in place (see Fig. 1c and Supplementary Fig. S6 for detailed geometry). To assess the ability of the aligned MRE-based metamaterial to generate highly tunable low-frequency bandgaps, a series of numerical simulations are carried out using a tailored finite element model which adequately captures the dissipative dynamics of the magnetorheological material (see the Simulations section for details). Figure 4e displays the wave dispersion diagram of the unit cell in the absence of a magnetic field, for both in- and out-of-plane modes. A local

resonance BG can be spotted from 192 to 270 Hz for out-of-plane deformations. Figure 4b shows the deformed metamaterial at 200 Hz for two distinct scenarios in response to an actuation at the far left end of the structure close to the clamped boundary: Sim 2 represents the case when the metamaterial is stimulated by a 1600 Oe magnetic field strength, and Sim 1 represents a control test in the absence of magnetic field. Spatial wave absorption along the propagation direction in Sim 1 confirms the local resonance BG predicted in Fig. 4e, and the end-to-end transmission in Sim 2 implies a shift in BG frequency as a result of the applied magnetic field, which forces 200 Hz outside the BG region. An experimental realization of the MRE-based metamaterial was fabricated and tested as illustrated in Fig. 4c (see the Metamaterial experiments section and Supplementary Figs. S4 through S6 for further details). Two arrays of permanent magnets were mounted facing each other and used to impose a uniform magnetic field on the aligned MRE fillers. Note that the distance between the magnets, and consequently, the strength of the generated magnetic field, are tunable enabling the reproduction of the experiments for different sets of parameters. To quantify the BG shift, a series of frequency sweeps were carried out. A transfer function between the out-of-plane displacement of the tip node (P2 in Fig. 4c) and the metamaterial base (P1 in Fig. 4c) was defined and measured. The transfer functions are plotted for both simulations and experiments in Fig. 4d. The rows of Fig. 4d correspond to different magnetic field strengths which are induced by changing the gap between the magnet faces as
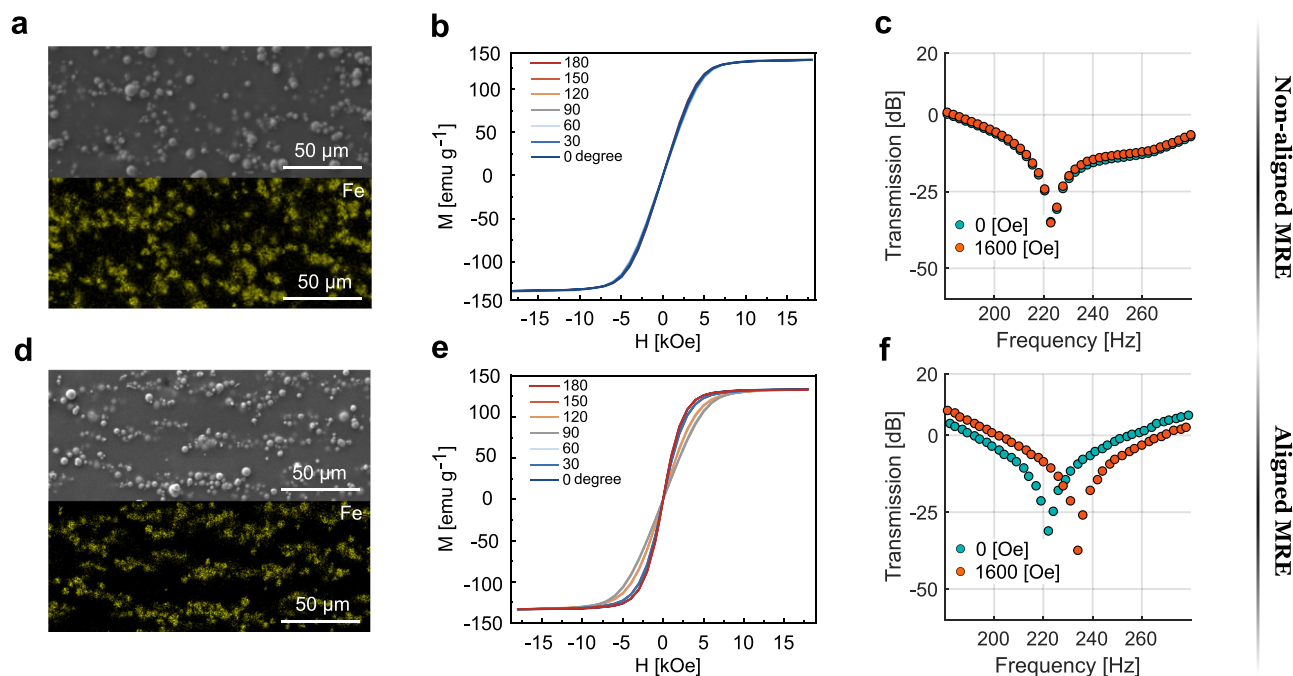
Fig. 2 Anisotropy in non-aligned versus aligned MRE samples. a, **d** SEM images (top half) and EDS mappings (bottom half) for the non-aligned and aligned MREs, respectively. **b**, **e** M–H loops at different angles for the non-aligned and aligned MREs, respectively. 0° corresponds to the measuring magnetic field being parallel to the aligned magnetic field. **c**, **f** The transmission spectrum of MRE-based metamaterials using the non-aligned and aligned MREs, respectively, in the absence (0 Oe) and presence (1600 Oe) of a magnetic field. A bandgap shift is hardly noticeable in (**c**) (non-aligned) and is significantly pronounced in (**f**) (aligned).
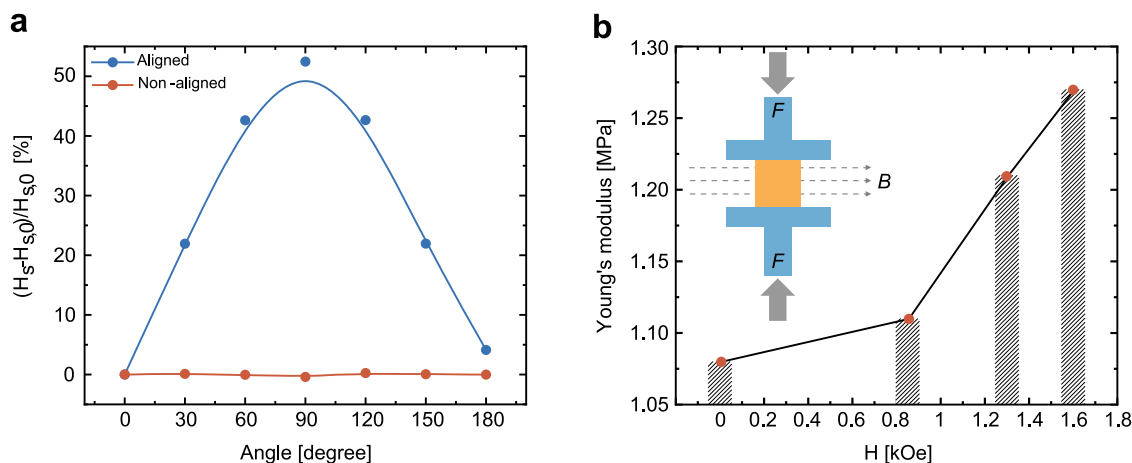

Fig. 3 Magneto-mechanical coupling. a Angle-dependent saturation magnetic field change for aligned and non-aligned MREs. In the aligned case, $H_{s,0}$ refers to the saturation magnetic field when the measuring magnetic field is parallel to the aligned one. **b** Dependence of the elastic (Young's) modulus on the magnetic field for the aligned MRE. Inset shows a schematic of the compression test under a magnetic field. F represents the compression force and B represents the magnetic field provided by permanent magnets.

illustrated in Fig. 4f. As the gap is gradually reduced, the aligned MRE filler becomes stiffer, eventually resulting in a noticeable BG shift to higher frequencies (highlighted region in Fig. 4d). For comparison, the results of Sim 1 and Sim 2 in Fig. 4b are indicated on the first and last rows of Fig. 4d, respectively, confirming a decent agreement between theory and physical testing. $\gamma_S = (f_S - f_{S0})/f_{S0}$ and $\gamma_E = (f_E - f_{E0})/f_{E0}$ are defined as the percentage normalized changes in the starting and ending BG frequencies, respectively, where f_S and f_E are the starting and ending BG frequencies in the presence of magnetic field and f_{S0} and f_{E0} are the starting and ending BG frequencies in the absence thereof, respectively. Figure 4g depicts the variation of these two metrics for different magnet gaps revealing the increasing

tunability of the metamaterial at stronger magnetic fields. Using numerical simulations, Fig. 5 demonstrates two different pathways to enhance the metamaterial's tunability beyond the best possible experimental performance (marked by point A in Fig. 5a). In the first approach, the effect of a stronger magnetic field on further boosting the MRE's Young's modulus while keeping the same level of anisotropy is evaluated. This corresponds to a shift from point A (peak experimental performance; $H = 1600$ Oe) to points B ($H = 2000$ Oe) and C ($H = 3000$ Oe) along the solid black curve, which indicates the experimentally-obtained level of anisotropy from the curing process. In the second approach, higher and lower levels of anisotropy are envisioned while keeping the strengths of magnetic field
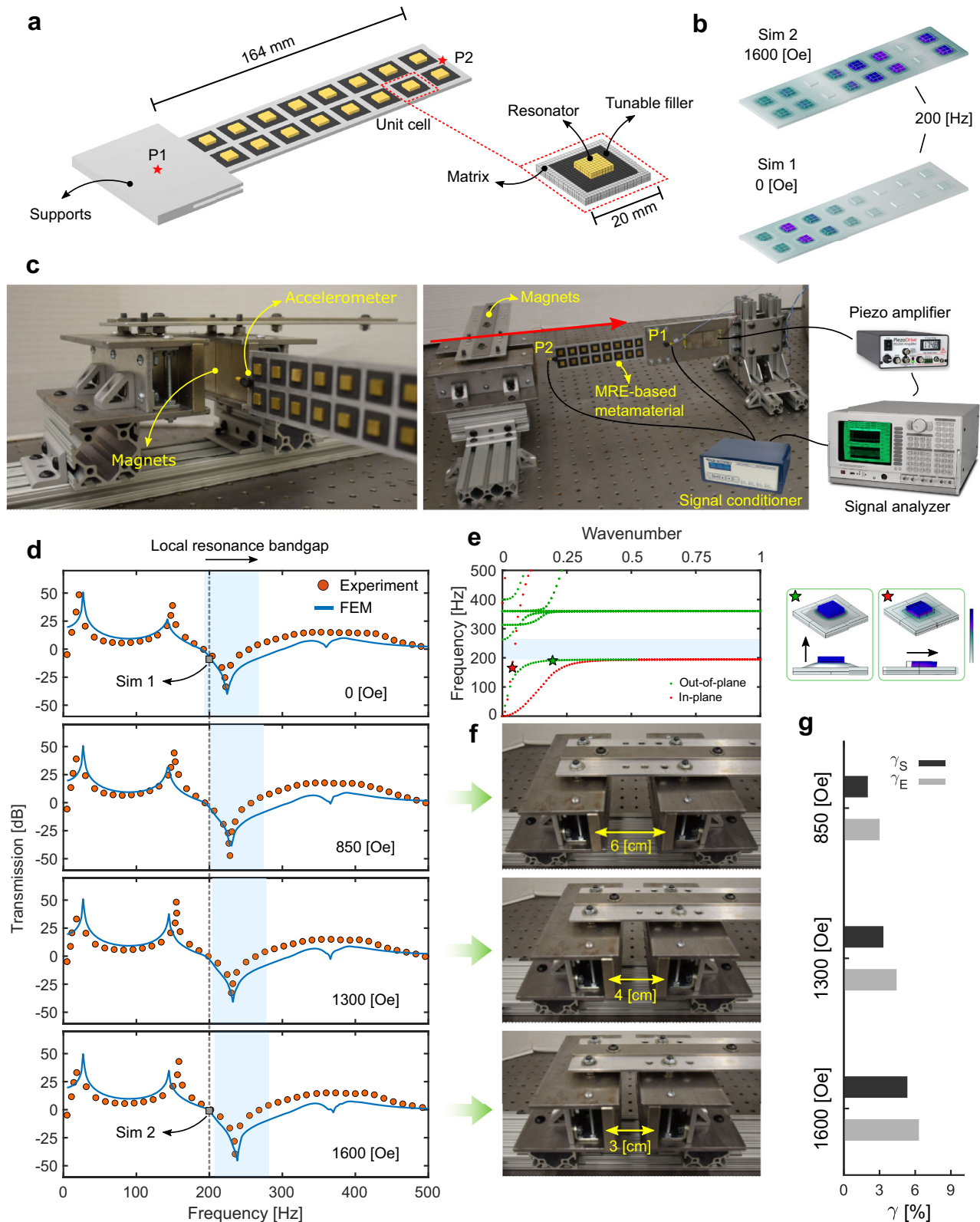
Fig. 4 Local resonance bandgap control in an aligned MRE-based metamaterial. a Metamaterial components, sensor locations, and geometric parameters.
b Out-of-plane displacement field at 200 Hz in the absence of a magnetic field (Sim 1) and at a magnetic field strengths of 1600 Oe (Sim 2). **c** Experimental apparatus.
Out-of-plane measurements at the locations of P1 and P2 are used to generate a transmission transfer function over the desired frequency range. **d** Transmission
spectrum from simulations (line) and experiments (scattered points) corresponding to magnetic field strength of (from top to bottom) 0, 850, 1300, and 1600 Oe.
Shaded area denotes bandgap region in each case as predicted from Bloch-wave analysis. **e** Unit cell dispersion diagram in the absence of magnetic field (reference
case). Shaded area denotes the field-free bandgap region. Side insets depict examples of out-of-plane and in-plane deformations. **f** Magnetic field variation mechanism
via adjustable gaps between facing permanent magnets. The shown distances correspond to the transmission plots in the adjacent rows of (**d**). **g** Percentage
normalized change in the starting γ_S and ending γ_E bandgap frequencies as a function of the applied magnetic field, corresponding to the different rows of (**d**) and (**f**).
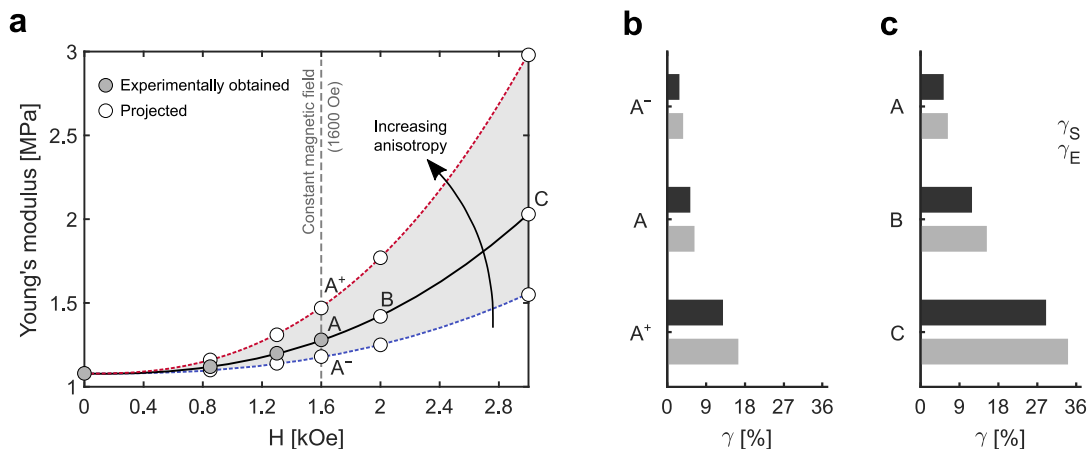
Fig. 5 MRE-based metamaterial with enhanced tunability. a Experimental and projected dependence of the elastic (Young's) modulus on the magnetic field for MREs with different levels of anisotropy. Point A marks peak experimental performance shown in Fig. 4. **b** Percentage normalized change in the starting γ_S and ending γ_E bandgap frequencies for experimentally obtained (solid black), superior (dashed red), and inferior (dashed blue) anisotropy levels at a constant magnetic field of 1600 Oe. **c** Percentage normalized change in the starting γ_S and ending γ_E bandgap frequencies corresponding to an increase in magnetic field beyond experimental limits, at the same anisotropy level of the MRE material.

unchanged. This corresponds to a vertical shift from point A to points A^+ and A^- on the red and blue dashed curves, respectively. In both scenarios, the percentage normalized change in the starting γ_S and ending γ_E bandgap frequencies, as defined earlier, is computed and shown in Fig. 5b, c.

Conclusion

From fabrication to dynamical testing, this paper demonstrated an experimental pathway to achieving a robust MRE-based magnetically programmable metamaterial through magnetic anisotropy and particle alignment. In contrast to current configurations of stimuli-responsive metamaterials where the distribution of ferromagnetic particles is uniform in the elastomeric medium, the predominantly anisotropic MRE-filler used here as the elastic component of the metamaterial cell exploits the enhanced stiffness tunability stemming from the ferromagnetic particles being constrained and coerced into aligning with the applied magnetic field during the curing process. Through a series of simulations and experiments, it was demonstrated that such alignment significantly strengthens magneto-mechanical coupling in the MRE fillers and builds up ability of the emergent local resonance bandgaps to be shifted and moved along the frequency axis via an external magnetic field. The results and experimental framework shown here promote the use of MREs in the design of active metamaterials and set a roadmap for broader future implementations.

Methods

Materials. The magnetorheological elastomers were made with 70 wt% ferromagnetic particles (carbonyl iron particles, Sigma-Aldrich), 15 wt% additives (silicone oil, Fisher Chemical), and elastomer matrix (15 wt% silicone rubber, RTV). The carbonyl iron particles were mixed with silicone oil and silicone rubber to form an uncured MRE precursor. After uniformly mixed, the uncured MRE precursor was placed in a vacuum chamber (1 Pa) for one hour to remove the air inside the precursor. The non-aligned MRE sample was obtained by curing the MRE precursor in a 3D-printed mold for 48 hours. The aligned MREs were obtained by curing the samples in a 3D-printed mold under a magnetic field which is generated by arrays of permanent magnets. The maximum magnetic field during the curing process was about 3000 Oe.

Measurements. SEM and EDS measurements were recorded by field emission SEM (Hitachi S4000). Magnetic measurements were carried out using a vibrating sample magnetometer (VSM, MicroSense EZ7-380V). Compression experiments were carried out by a Mark-10 universal testing machine at room temperature (see Supplementary Note 4 for effect of sample geometry on the measurements). The magnetic field is applied through two neodymium magnets with a size of $50 \times 25 \times 10$ mm. The magnetic field strength was controlled by changing the gap distance between neodymium magnets.

Metamaterial experiments. A support system was designed to attach the metamaterial to an optical vibrationally-damped table. A nearly uniform magnetic field was realized facing 2 arrays of 6 permanent neodymium magnets (see Fig. 4c). Magnetic field strength of the constructed sliding assembly was tuned by changing the gap distance between faces of the arrays. The proposed design is capable of applying uniform magnetic field to all fillers along the metamaterial (see Supplementary Note 3 for details on magnetic field measurements). Static deflection of the metamaterial due to gravity was found to be insignificant due to the light weight of the individual unit cells (4.3 g) and no noticeable deformation of the elastomeric matrix was observed upon connecting the beam in a cantilevered setting to the test fixture. A signal generator (Stanford Research Systems SR780) was used to perform a frequency sweep, 0–500 Hz, with a resolution of 0.5 Hz. The generated harmonic signal was amplified (PiezoDrive PD200) and fed to a pair of extender piezoelectric wafers which were attached to opposite faces of the metamaterial. A flexural wave was realized via an out of phase 180° excitation of these piezoelectric wafers. A pair of accelerometers (PCB Piezotronics 352A24) was used to measure the out-of-plane deformations of the structure. A transfer function was defined between the out-of-plane displacement of the tip and the base of the metamaterial. For dimensions and geometric details of the fabricated metamaterial, refer to Supplementary Fig. S6.

Simulations. Finite element simulations were carried out using the structural mechanics module of COMSOL Multiphysics. The proposed metamaterial was modeled using 3D elements comprised of three different materials: An aluminum matrix ($E = 68.9$ GPa, $\rho = 2700$ kg/m^3, and $v = 0.33$), a brass core ($E = 106$ GPa, $\rho = 8500$ kg/m^3, and $v = 0.32$), and an MRE filler

($\rho = 2444 \, kg/m^3$ and $v = 0.4$). The extent of frequency-dependence of the elastic modulus of MREs ranges from mild[41,42] to strong[38], it varies from one elastomer to another and is typically more pronounced at higher frequencies. To capture the viscoelastic behavior of the MRE filler used in this study, experimental measurements of the real and imaginary components of the elastic modulus (i.e., storage and loss moduli[43]) were carried out via a Dynamic Mechanical Analyzer (DMA850 from TA Instruments) as detailed in Supplementary Note 6. Supplementary Fig. S11 depicts the variation of the material's elastic modulus and loss factor over the intended frequency range of 0–500 Hz. Although variation is found to be minimal, the experimental values are incorporated in all numerical simulations. The procedure used to generate the dispersion diagrams of a unit cell with frequency-dependent material properties is detailed in Supplementary Note 6, since a traditional wavenumber-to-frequency approach does not allow for frequency-dependent elastic modulus values to be set a priori[44]. To generate the FRF plots, a frequency domain analysis was performed using a single excitation in the form of a transverse z-directional displacement at the far left end of the metamaterial, near the clamped boundary. A tip-to-base displacement transfer function was defined corresponding to the locations of the experimental measurements. To account for different magnetic configurations, the effect of the magnetic field strength levels is explicitly considered as the corresponding change in the filler's elastic modulus as quantified by the experimental measurements.

Data availability
The authors declare that the data supporting the findings of this study are available within the paper, and its supplementary information files.

References
1. Zhou, X., Liu, X. & Hu, G. Elastic metamaterials with local resonances: an overview. *Theor. Appl. Mech. Lett.* **2**, 041001 (2012).
2. Hussein, M. I., Leamy, M. J. & Ruzzene, M. Dynamics of phononic materials and structures: Historical origins, recent progress, and future outlook. *Appl. Mech. Rev.* **66**, 040802 (2014).
3. Zhai, Y., Kwon, H.-S. & Popa, B.-I. Anomalous reflection with omnidirectional active metasurfaces operating in free space. *Phys. Rev. Appl.* **16**, 034023 (2021).
4. Hathcock, M., Popa, B.-I. & Wang, K. Origami inspired phononic structure with metamaterial inclusions for tunable angular wave steering. *J. Appl. Phys.* **129**, 145103 (2021).
5. Lin, Z., Zhang, Y., Wang, K. & Tol, S. Anomalous wavefront control via nonlinear acoustic metasurface through second-harmonic tailoring and demultiplexing. *Appl. Phys. Lett.* **121**, 201703 (2022).
6. Moghaddaszadeh, M., Adlakha, R., Attarzadeh, M., Aref, A. & Nouh, M. Nonreciprocal elastic wave beaming in dynamic phased arrays. *Phys. Rev. Appl.* **16**, 034033 (2021).
7. Lin, Z., Al Ba'ba'a, H. & Tol, S. Piezoelectric metastructures for simultaneous broadband energy harvesting and vibration suppression of traveling waves. *Smart Mater. Struct.* **30**, 075037 (2021).
8. Zangeneh-Nejad, F., Sounas, D. L., Alù, A. & Fleury, R. Analogue computing with metamaterials. *Nat. Rev. Mater.* **6**, 207–225 (2021).
9. Attarzadeh, M., Callanan, J. & Nouh, M. Experimental observation of nonreciprocal waves in a resonant metamaterial beam. *Phys. Rev. Appl.* **13**, 021001 (2020).
10. Sigalas, M. & Economou, E. N. Band structure of elastic waves in two dimensional systems. *Solid State Commun.* **86**, 141–143 (1993).
11. Liu, Z. et al. Locally resonant sonic materials. *science* **289**, 1734–1736 (2000).
12. Beli, D., Arruda, J. & Ruzzene, M. Wave propagation in elastic metamaterial beams and plates with interconnected resonators. *Int. J. Solids Struct.* **139**, 105–120 (2018).
13. DePauw, D., Al Ba'ba'a, H. & Nouh, M. Metadamping and energy dissipation enhancement via hybrid phononic resonators. *Extrem. Mech. Lett.* **18**, 36–44 (2018).
14. Stein, A., Nouh, M. & Singh, T. Widening, transition and coalescence of local resonance band gaps in multi-resonator acoustic metamaterials: From unit cells to finite chains. *J. Sound Vib.* **523**, 116716 (2022).
15. Pratapa, P. P., Suryanarayana, P. & Paulino, G. H. Bloch wave framework for structures with nonlocal interactions: application to the design of origami acoustic metamaterials. *J. Mech. Phys. Solids* **118**, 115–132 (2018).
16. Al Ba'ba'a, H., DePauw, D., Singh, T. & Nouh, M. Dispersion transitions and pole-zero characteristics of finite inertially amplified acoustic metamaterials. *J. Appl. Phys.* **123**, 105106 (2018).
17. Popa, B.-I., Zigoneanu, L. & Cummer, S. A. Tunable active acoustic metamaterials. *Phys. Rev. B* **88**, 024303 (2013).
18. Ragonese, A. & Nouh, M. Prediction of local resonance band gaps in 2D elastic metamaterials via Bloch mode identification. *Wave Motion* **105**, 102734 (2021).
19. Kheybari, M., Wang, Z., Xu, H. & Bilal, O. R. Programmability of ultrathin metasurfaces through curvature. *Extrem. Mech. Lett.* **52**, 101620 (2022).
20. Liu, H., Wu, J. H. & Ma, F. Dynamic tunable acoustic metasurface with continuously perfect sound absorption. *J. Phys. D* **54**, 365105 (2021).
21. Willey, C., Chen, V., Scalzi, K., Buskohl, P. & Juhl, A. A reconfigurable magnetorheological elastomer acoustic metamaterial. *Appl. Phys. Lett.* **117**, 104102 (2020).
22. Thomes, R. L., Beli, D. & Junior, C. D. M. Space–time wave localization in electromechanical metamaterial beams with programmable defects. *Mech. Syst. Signal Process.* **167**, 108550 (2022).
23. Callanan, J. et al. Uncovering low frequency band gaps in electrically resonant metamaterials through tuned dissipation and negative impedance conversion. *Smart Mater. Struct.* **31**, 015002 (2021).
24. Chen, X. et al. Active acoustic metamaterials with tunable effective mass density by gradient magnetic fields. *Appl. Phys. Lett.* **105**, 071913 (2014).
25. Hu, Y. et al. A 3D-printed molecular ferroelectric metamaterial. *Proc. Natl Acad. Sci. USA* **117**, 27204–27210 (2020).
26. Ginder, J. M., Nichols, M. E., Elie, L. D. & Tardiff, J. L. Magnetorheological elastomers: properties and applications. In *Smart Structures and Materials 1999: Smart Materials Technologies*, vol. 3675, 131–138 (SPIE, 1999).
27. Bastola, A. K. & Hossain, M. A review on magneto-mechanical characterizations of magnetorheological elastomers. *Compos. Part B* **200**, 108348 (2020).
28. Liao, G., Gong, X., Xuan, S., Kang, C. & Zong, L. Development of a real-time tunable stiffness and damping vibration isolator based on magnetorheological elastomer. *J. Intell. Mater. Syst. Struct.* **23**, 25–33 (2012).
29. Li, W., Zhang, X. & Du, H. Magnetorheological elastomers and their applications. In *Advances in elastomers I*, 357–374 (Springer, 2013).
30. Yu, K., Fang, N. X., Huang, G. & Wang, Q. Magnetoactive acoustic metamaterials. *Adv. Mater.* **30**, 1706348 (2018).
31. Harne, R. L., Deng, Z. & Dapino, M. J. Adaptive magnetoelastic metamaterials: a new class of magnetorheological elastomers. *J. Intell. Mater. Syst. Struct.* **29**, 265–278 (2018).
32. Bayat, A. & Gordaninejad, F. Band-gap of a soft magnetorheological phononic crystal. *J. Vib. Acoust.* **137**, 011011 (2015).
33. Zhang, G. & Gao, Y. Tunability of band gaps in two-dimensional phononic crystals with magnetorheological and electrorheological composites. *Acta Mech. Solid Sin.* **34**, 40–52 (2021).
34. Ansari, M., Attarzadeh, M., Nouh, M. & Karami, M. A. Application of magnetoelastic materials in spatiotemporally modulated phononic crystals for nonreciprocal wave propagation. *Smart Mater. Struct.* **27**, 015030 (2017).
35. Yan, W., Zhang, G. & Gao, Y. Investigation on the tunability of the band structure of two-dimensional magnetorheological elastomers phononic crystals plate. *J. Magn. Magn. Mater.* **544**, 168704 (2022).
36. Xu, Z., Tong, J. & Wu, F. Magnetorheological elastomer vibration isolation of tunable three-dimensional locally resonant acoustic metamaterial. *Solid State Commun.* **271**, 51–55 (2018).
37. Liu, S., Zhao, Y., Zhao, D., Wu, J. & Gao, C. Tunable elastic wave bandgaps and waveguides by acoustic metamaterials with magnetorheological elastomer. *Acoust. Phys.* **66**, 123–131 (2020).
38. Pierce, C. D. et al. Adaptive elastic metastructures from magneto-active elastomers. *Smart Mater. Struct.* **29**, 065004 (2020).
39. Zhang, K., Jiao, W. & Gonella, S. Tunable band gaps and symmetry breaking in magnetomechanical metastructures inspired by multilayer two-dimensional materials. *Phys. Rev. B* **104**, L020301 (2021).
40. Bica, I. The influence of the magnetic field on the elastic properties of anisotropic magnetorheological elastomers. *J. Ind. Eng. Chem.* **18**, 1666–1669 (2012).
41. Boczkowska, A., Awietjan, S. F., Pietrzko, S. & Kurzydłowski, K. J. Mechanical properties of magnetorheological elastomers under shear deformation. *Compos. Part B* **43**, 636–640 (2012).
42. Burhannuddin, N. L. et al. Physicochemical characterization and rheological properties of magnetic elastomers containing different shapes of corroded carbonyl iron particles. *Sci. Rep.* **11**, 868 (2021).

43. Akl, W., Nouh, M., Aldraihem, O. & Baz, A. Energy dissipation characteristics of polyurea and polyurea/carbon black composites. *Mech. Time Depend. Mater.* **23**, 223–247 (2019).

44. Nouh, M. A., Aldraihem, O. J. & Baz, A. Periodic metamaterial plates with smart tunable local resonators. *J. Intell. Mater. Syst. Struct.* **27**, 1829–1845 (2016).

Acknowledgements

Author contributions

A.A., C.Z., S.R., and M.N. designed and supervised the research. Y.H. and Z.G. performed the fabrication and magnetic alignment. Y.H. measured the magnetic properties, magneto-mechanical coupling and performed SEM. M.M. and A.R. built the experimental setup and carried out Doppler vibrometry and dynamic testing. All authors analyzed the data. The paper was written with input from all authors.

Competing interests

The authors declare no competing interests.

Additional information

Supplementary information The online version contains supplementary material available at https://doi.org/10.1038/s43246-023-00419-7.

Correspondence and requests for materials should be addressed to Mostafa Nouh.

Peer review information *Communications Materials* thanks Kun-Hao Yu and the other, anonymous, reviewer(s) for their contribution to the peer review of this work. Primary Handling Editor: Aldo Isidori.

Reprints and permission information is available at http://www.nature.com/reprints

Publisher's note Springer Nature remains neutral with regard to jurisdictional claims in published maps and institutional affiliations.